Topological aspects responsible for recrystallization evolution in an IF-steel sheet – Investigation with cellular-automaton simulations

Traka, Konstantina; Sedighiani, Karo; Bos, Cornelis; Galan Lopez, Jesus; Angenendt, Katja; Raabe, Dierk; Sietsma, Jilt

DOI
10.1016/j.commatsci.2021.110643

Publication date
2021

Document Version
Final published version

Published in
Computational Materials Science

Computational Materials Science 198 (2021) 110643

Contents lists available at ScienceDirect

Computational Materials Science

journal homepage: www.elsevier.com/locate/commatsci

Topological aspects responsible for recrystallization evolution in an IF-steel sheet – Investigation with cellular-automaton simulations

Konstantina Traka [a,b,*], Karo Sedighiani [a,b], Cornelis Bos [a,c], Jesus Galan Lopez [a], Katja Angenendt [b], Dierk Raabe [b], Jilt Sietsma [a]

[a] Department of Materials Science and Engineering, TU Delft, Mekelweg 2, Delft 2628 CD, The Netherlands
[b] Max-Planck-Institut für Eisenforschung GmbH, Max-Planck-Straß 1, 40237 Düsseldorf, Germany
[c] Tata Steel Europe, IJmuiden, The Netherlands

ARTICLE INFO

Keywords:
Recrystallization
Cellular-Automaton
Abnormal subgrain growth
IF-steel
Shear band nucleation

ABSTRACT

A cellular automaton algorithm for curvature-driven coarsening is applied to a cold-rolled interstitial-free steel's microstructure - obtained through electron backscatter diffraction (EBSD). Recrystallization nucleation occurs naturally during the simulation, due to the highly heterogeneous and hence competitive growth among pre-existing (sub) grains. The spatial inhomogeneity of the subgrain growth that takes place derives from the large local variations of subgrain sizes and misorientations that comprise the prior deformed state. The results show that capillary-driven selective growth takes place to the extent that the prior elongated and deformed grains are replaced by equiaxed grains with no interior small-angle boundaries. Additionally, during the simulation certain texture components intensify and others vanish, which indicates that preferential growth occurs in a fashion that relates to the crystal orientations' topology. The study of the early stages of recrystallization (i.e. nucleation) shows that the pre-existing subgrains that eventually recrystallize, exhibit certain topological characteristics at the prior deformed state. Successful nucleation occurs mostly for pre-existing matrix subgrains abutting shear bands or narrow deformation bands and particularly at regions where the latter intersect.

1. Introduction

1.1. Motivation

Recrystallization has been extensively studied in low carbon (LC) and interstitial-free (IF) steels [1–18]. Besides the experimental work, the topological mesoscopic computation of recrystallization related phenomena has also helped to understand the mechanisms responsible for the microstructural processes that occur [19–28]. Although the origin of recrystallization nuclei in such metals has been well-explained by the subgrain formation and growth mechanism [29–36], the early stages of recrystallization comprise a still unresolved matter [6]. This is because there are many interacting boundaries and microstructural features (e.g. shear bands and grain boundaries) and numerous concurring mechanisms related to the onset of recrystallization [5,31]. Hence, it has not been clarified why particular subgrains evolve into recrystallization nuclei and others for example do not.

The goal of this work is to study how the local topology can contribute to the nucleation and growth of pre-existing subgrains. Investigating the early stages of recrystallization requires the simulation of the coarsening that occurs in all subgrains simultaneously – see for example the studies of Rollett and Holm [33] and Han et al. [37]. Therefore, we simulated recrystallization in a Ti-stabilized IF steel cold-rolled at 77% thickness reduction and we allowed all pre-existing subgrains to compete in evolving into recrystallized grains. In other words, nucleation in this work is not artificially imposed but evolves out of the discontinuous competitive subgrain coarsening process, as explained by Humphreys [38]. We used a close coupling to the inherited microstructure and thereby investigated the topological characteristics that facilitate recrystallization initiation and growth.

1.2. Relationship between inhomogeneous subgrain coarsening and recrystallization

At the mesoscopic scale, recrystallization in highly plastically strained metals is normally described as a process comprising successive

* Corresponding author at: Department of Materials Science and Engineering, TU Delft, Mekelweg 2, Delft 2628 CD, The Netherlands.
E-mail address: C.Traka@tudelft.nl (K. Traka).

https://doi.org/10.1016/j.commatsci.2021.110643
Received 5 December 2020; Received in revised form 3 June 2021; Accepted 4 June 2021
Available online 29 June 2021

interface phenomena referred to as nucleation and growth. However, it has been well-established that in materials that tend to form subgrain structures[1], recrystallization phenomena proceed through a mostly heterogeneous (sub) grain growth process [5,8,9,14,29–32,36–44]. Some of the pre-existing subgrains grow (while others shrink), gradually accumulate increasing misorientation and/or size relative to their changing neighborhood, and finally recrystallize.

In this view, recrystallization can be described as a phenomenon physically related to grain coarsening, particularly the one known as discontinuous/abnormal (sub) grain growth [33,38]. The restoration process involved in all stages of recrystallization is described by the reduction of (sub) boundary energy. Hence, the stored deformation energy is approximated from the dislocation content at the boundaries i.e. high angle grain boundaries (HAGBs) and geometrically necessary dislocations (GNDs). Although statistically stored dislocations (SSDs) may highly contribute to the material's stored energy, metals characterized by high stacking fault energy (SFE), such as iron and aluminum, form subgrain structures usually already during the plastic deformation process. This is due to the high mobility and cross-slip frequency of the dislocations [2]. The predominance of subgrain structures in such metals has been revealed by numerous investigations [2,8,9,45–49] using transmission electron microscopy (TEM) after cold deformation.

Although the description of recrystallization-related phenomena as a capillary competitive (sub) grain growth mechanism is an approximation, it nonetheless unifies the stages of nucleation, recrystallization growth and grain growth into one physics-based framework – as suggested by Humphreys [38] – and thereby enables their simultaneous computation. The relevant terminology which we have followed in this paper is presented in Table 1. We adopted the terms primarily from [38] and additionally from [2,33,39,40,51].

The capillary competitive (sub) grain growth modeling approach suggests that the heterogeneity in the subgrains' coarsening stems from the heterogeneous distribution of the orientation gradients (i.e. GNDs and HAGBs) [33,38]. These determine the mobility and the driving force whereby subgrain growth occurs [52–54]. Accumulating enough mobility (due to growing misorientation when absorbing the lattice spin from other cells) and/or higher driving forces gives an advantage to some subgrains and this is called nucleation [2.33.38,39,51]. Hence, although nucleation is not artificially imposed in this work, it evolves naturally out of the evolving substructure, by the mechanisms known as discontinuous subgrain growth [5] and HAGB bulging [32]. Both nucleation mechanisms are relevant to the recrystallization of cold-worked IF-steel in the range of 70–80% thickness reduction [5,25,28,31]. Other possibly relevant mechanisms such as subgrain coalesence [55,56], heterogeneous static subgrain formation [57,58], variations of particle pinning at certain HAGBs [11,52,59–62] are not addressed in this work. Although such processes may contribute to the nucleation and growth of recrystallization by providing a kinetic or size advantage to some subgrains, our aim is to investigate the effect and spatial variation of the curvature-driven motion.

Table 1
Terminology used in the document.

Term	Description
Kinetically unstable boundary	A boundary which has high mobility, compared to most boundaries in the microstructure at that time e.g. in the current application the term applies to a HAGB.
Thermodynamically unstable boundary	A boundary which yields energy release upon an incremental migration.
Kinetic advantage (of a subgrain or grain)	A (sub)grain that continues being surrounded by large angle boundaries after initiating recrystallization.
Thermodynamic/size/energy advantage (of a subgrain or grain)	A (sub)grain that continues being larger from the subgrains it meets during its expansion after initiating recrystallization.
Recrystallization nucleation	When a subgrain is particularly competitive and has grown enough so that the recrystallized volume can be clearly distinguished from the surrounding substructure, it is considered as nucleus.

[1] Materials form subgrain structures when dislocations can undergo cross-slip and climb during deformation. Therefore such structures predominate in metals characterized by high stacking fault energy (SFE) and in sheets deformed at high temperatures.

[2] Even if the substructure is not fully recovered in the as-deformed state, static recovery will still take place (both as polygonization [34–36] and dislocation annihilation) in the very early stages of annealing and thereby diminish the "free" dislocations' content.

1.3. Implementation

The algorithm is implemented in the simulation package CASIPT [63,64] (Cellular Automata Sharp Interface Phase Transformations) based on the deterministic CA method presented in [65]. We used an experimentally measured and highly resolved representative volume element (RVE), in which intergranular aspects (e.g. shear and deformation bands) can be distinguished, and orientation gradients within grains are described. The RVE was obtained through electron backscatter diffraction (EBSD).

The misorientation between adjacent pixels identified by the EBSD is attributed to the existence of dislocations. These incorporate the role of elementary units of inelastic deformation and hence they carry the deformation energy. At the same time, dislocations are elementary units of crystallographic misorientation and hence comprise boundaries whereby (sub) grains can grow. Therefore, the dislocation content identified by the EBSD determines the kinematics (mobility) and the stored energy (driving force) whereby recrystallization is simulated.

It should be made clear that the EBSD measurement we used, albeit high in resolution – namely 0.12 μm – cannot describe all the orientation gradients in the substructure. Typical subgrain sizes that have been reported from TEM measurements in cold-rolled IF-steels of 70–80% thickness reduction, are found within a range of 0.4–1 μm [1,66–68]. Hence most of the subgrain structure can be described with the present resolution, although regions of very high orientation gradients may still accommodate smaller subgrains.

2. Model description

2.1. Constitutive state variables used in the automaton grid

In the automaton grid every cell i is assigned a crystal orientation g_i. The algorithm considers the 1st Von-Neumann neighborhood (see [65,69]). Each boundary area between material volumes i and j carries an interfacial energy value equal to:

$$E_{ij}[\mathrm{J}] = \gamma(g_i, g_j)\cdot A_{ij} \quad \forall\ ij : \delta_{ij} = 0 \tag{1}$$

where in Eq. (1):

- $A_{ij}[\mathrm{m}^2]$ is the area of the boundary's ij plane
- $\gamma(g_i, g_j)[\mathrm{J/m}^2]$ is the interface energy density between two unlike adjacent orientations g_i, g_j
- δ_{ij} is a Kronecker-like operator defined as:

$$\delta_{ij} = \begin{cases} 1 & \text{if } \theta_{ij} < \theta_{min} \\ 0 & \text{if } \theta_{ij} >= \theta_{min} \end{cases} \tag{2}$$

where in Eq. (2):

- $\theta_{ij}[^\circ]$ is the misorientation between orientations g_i and g_j
- $\theta_{min}[^\circ]$ is the lower cut-off misorientation to consider the existence of a boundary between i and j

Low angle grain boundaries (LAGBs) carry essentially an elastic energy density which is ascending to the misorientation as follows [70]:

$$\gamma(g_i, g_j) = \begin{cases} \gamma_{HAGB} & \text{if } \theta_{ij} \geqslant \theta_{HAGB} \\ \gamma_{HAGB} \cdot \frac{\theta_{ij}}{\theta_{HAGB}} \cdot \left(1 - \ln\left(\frac{\theta_{ij}}{\theta_{HAGB}}\right)\right) & \text{if } \theta_{ij} < \theta_{HAGB} \end{cases} \quad (3)$$

where in Eq. (3):

- $\theta_{HAGB}[^\circ]$ is the lower threshold misorientation to consider a HAGB

2.2. Incremental energy release during kinetic evolution of the CA

2.2.1. Expression

If the automaton cell i with orientation g_i, is swept by its neighbor cell j, it assumes the new orientation g_j. The energy change on cell's i neighborhood is calculated as:

$$\Delta E_{g_i \to g_j}\left[\mathrm{J}\right] = \sum_k A_{ik} \cdot \left(1 - \delta_{ik}\right) \cdot \gamma\left(g_i, g_k\right) - \sum_k \left(1 - c \cdot \delta_{lkij}\right) \cdot A_{ik} \cdot \left(1 - \delta_{jk}\right) \cdot \gamma\left(g_j, g_k\right) \quad (4)$$

where in Eq. (4):

- k are the cells with $A_{ik} \neq 0$ i.e. neighbours of cell i
- $c \in (0,1]$, is constant and it is related to the configuration of the grid

In Eq. (4) the energy states before and after the re-orientation are expressed in opposite order such that energy release yields a positive summation is $\Delta E_{g_i \to g_j}$. This convention was chosen in order to keep consistency with the terms used e.g. positive driving force.

The four indices' Kronecker-like operator δ_{lkij} and the constant c used in Eq. (4) are here introduced to account for the cases that two adjacent similarly oriented cells j and k may grow together. This assumption is made because long before cell j consumes cell i, a neighbour cell of the same orientation would have also started to grow toward its own closest neighbours. This is due to the high local curvature that would otherwise be created and "drag" the similarly oriented regions. When δ_{lkij} equals 1 it means that a neighbour cell l, which is oriented as j, can grow together with j cell to transform cell k. Cell k is another neighbour of cell i, thus the next state's energy reduces by $c \cdot \gamma(g_j, g_k) \cdot A_{ik}$, since a part of cell's k volume (defined as c) will have the same orientation with i, which is g_j. Cases where $\delta_{lkij} = 1$ are illustrated and explained in Fig. 1. The four indices' Kronecker-like operator used in Eq. (4) is then defined as:

$$\delta_{lkij} = \begin{cases} 1 & \text{if } \exists\ l\ :\ \overrightarrow{ji} = \overrightarrow{lk}\ \Lambda\ \delta_{jl} = 1\ \Lambda\ \delta_{lk} = 0 \\ 0 & \text{if not} \end{cases} \quad (5)$$

where in Eq. (5):

- $\overrightarrow{ji}$ is the position vector of cell's i center with respect to the center of cell j

2.2.2. Energy change – Examples

Fig. 1 shows a schematic for the two main switching scenarios that occur in the application. The color-coding of the cells is in accord with the Inverse-Pole-Figure (IPF) along the Normal Direction (ND). Boundary segments are also plotted when present, such that a HAGB is colored black and a LAGB blue. In particular:

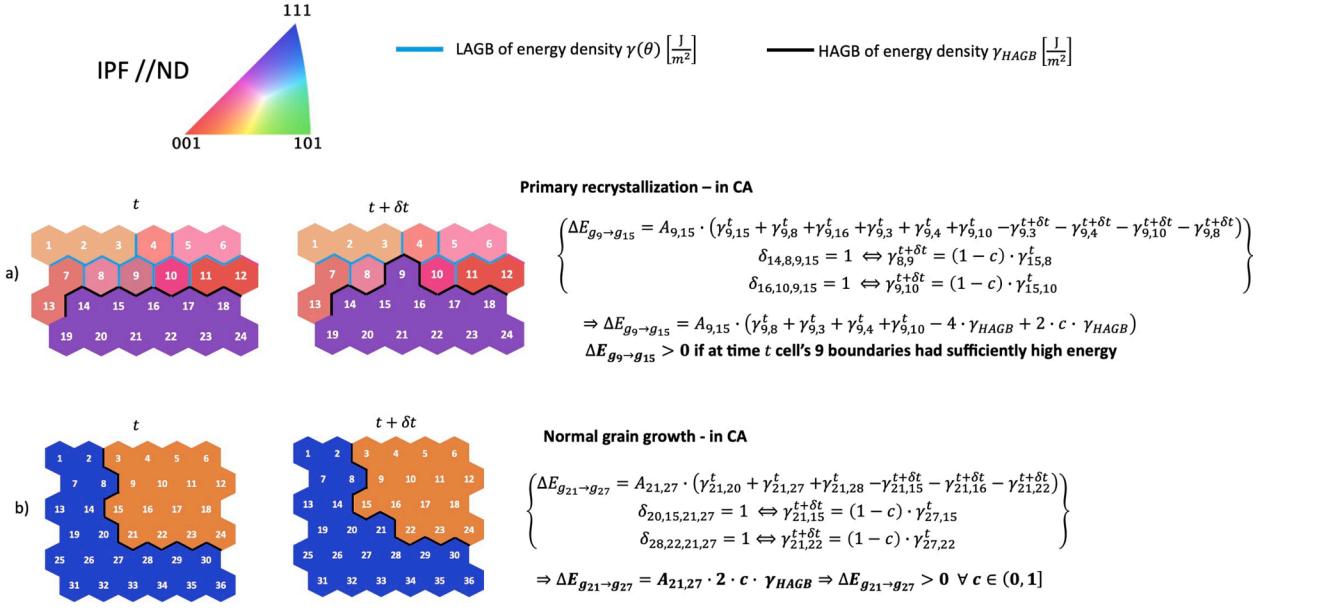

Fig. 1. Cell switching scenarios in the CA. The two main cases that will occur when the algorithm is applied to a deformed microstructure discretized in a 2D hexagonal automaton grid are shown. The images depict the energy state before and after the re-orientation. In Figure (a) cell 15 (growing cell) belongs to a recrystallized volume (or large subgrain next to a HAGB) and might grow into cell 9 that belongs to a substructure. Although the migration increases the HAGB area, a positive driving force can still be found since the LAGB area decreases. Also, cell 15 has neighbours (i.e. cells 14 and 16) of the same orientation which can grow in the same direction (i.e. toward cells 8 and 10, respectively). In this case, only a part (i.e. $1-c$) of the energy concerning the boundaries $9,8$ and $9,10$ is considered upon the calculation of the next state's energy if cell 9 re-orients. In Figure (b) cells 27 and 21 are both surrounded by some cells similarly oriented and hence positive driving force will only be found if the migration leads to reduction of the HAGB area. Therefore, the migration of the boundary $27,21$ will occur toward cell 21. Cell 27 has neighbours (i.e. cells 20 and 28) which can grow in the same direction i.e. toward cells 15 and 22, respectively. Therefore, again only $1-c$ of the boundaries' $21,15$ and $21,22$ energy is considered at the next state.

- Fig. 1a shows a typical example of primary recrystallization, where a strain-free grain (or large subgrain next to a HAGB) grows into the adjacent substructure. As is shown, although the motion is accompanied by an increase in the HAGB area, it reduces the LAGB area to the extent that it yields energy release.
- Fig. 1b shows a typical example of normal grain growth, where a grain favored by the HAGB curvature grows into a smaller one. As expected, for such growth to occur in the CA, the HAGB energy needs to decrease.

Hence, although recrystallization and grain growth are phenomenologically different, their physical description can be unified [38]. If there is sufficient difference in the dislocations' content per unit volume between two adjacent dissimilar cells, one will grow into the other.

Fig. 2 shows the two scenarios described in Fig. 1 as measured experimentally. Fig. 2a shows a recrystallized grain growing into a deformed grain. As was shown in Fig. 1a, in such cases, the HAGBs curvature normally does not favor the migration, yet orientation gradients within the deformed matrix can lead to a positive driving force. Fig. 2b shows two recrystallized grains where the curvature of the HAGB indicates the direction of growth, as also described in Fig. 1b.

2.3. Growth rate

If the energy change in Eq. (4) is positive (favorable migration) the boundary segment ij exerts a pressure to re-orient the adjacent cell's i volume V_i, which is equal to:

$$\Delta G_{g_i\to g_j}[\mathrm{J}/\mathrm{m}^3] = \Delta E_{g_i\to g_j}[\mathrm{J}]/V_i[\mathrm{m}^3] \tag{6}$$

The pressure displaces the boundary ij with velocity:

$$\begin{aligned} v_{g_i\to g_j}\left[\mathrm{m}/\mathrm{s}\right] &= M\left(g_i,g_j\right)\left[\mathrm{m}^4/\mathrm{Js}\right]\cdot\Delta G_{g_i\to g_j}\left[\mathrm{J}/\mathrm{m}^3\right] \Rightarrow^{(4),(6)} v_{g_i\to g_j}\left[\mathrm{m}/\mathrm{s}\right] \\ &= M\left(g_i,g_j\right)\cdot\left(\sum_k A_{ik}\cdot\left(1-\delta_{ik}\right)\cdot\gamma\left(g_i,g_k\right) - \sum_k\left(1 \right.\right. \\ &\left.\left. - c\cdot\delta_{lkij}\right)\cdot A_{ik}\cdot\left(1-\delta_{jk}\right)\cdot\gamma\left(g_j,g_k\right)\right)/V_i \end{aligned} \tag{7}$$

In Eq. (7) $M(g_i,g_j)$ is the boundary mobility [71] which depends on the boundary's misorientation (for LAGBs) as follows [39]:

$$M\left(g_i,g_j\right) = \begin{cases} M_{HAGB} & if\ \theta_{ij}\geq\theta_{HAGB} \\ M_{HAGB}\cdot\left(1-exp\left(-5\cdot\left(\dfrac{\theta_{ij}}{\theta_{HAGB}}\right)^4\right)\right) & if\ \theta_{ij}<\theta_{HAGB} \end{cases} \tag{8}$$

where in Eq. (8) M_{HAGB} is defined as [71]:

$$M_{HAGB}\left[\mathrm{m}^4/\mathrm{Js}\right] = M_0\cdot\exp\left(\frac{-Q_g}{\mathrm{R}\cdot T}\right) \tag{9}$$

where in Eq. (9):

- $Q_g[\mathrm{J/mol}]$ is the activation energy for the migration of a HAGB
- $\mathrm{R} = 8.314\ \mathrm{J/mol\cdot K}$ is the universal gas constant
- $T[\mathrm{K}]$ is the applied temperature
- $M_0[\mathrm{m}^4/\mathrm{Js}]$ is the pre-exponential factor

The pressure on the boundary ij imposes a force equal to:

$$\vec{F}_{ij,g_i\to g_j}\left[\mathrm{N}\right] = \Delta G_{g_i\to g_j}\cdot A_{ij}\cdot\vec{u}_{ji} \tag{10}$$

where in Eq. (10):

- $\vec{u}_{ji}$ is the unit vector normal to the plane ij

Every cell k which is neighbour to cell i and is misoriented less than θ_{min} from the growing orientation g_j (i.e. $\delta_{kj}=1$) will migrate toward cell i perpendicularly to the boundary's ik plane, with velocity given from Eq. (7) – i.e. the same as boundary's ij. Hence, the total force for re-orientation of a cell i results from all migrating boundaries and their relative direction, such that:

$$\begin{aligned} \vec{F}_{g_i\to g_j}\left[\mathrm{N}\right] &= \sum_k \delta_{kj}\cdot\vec{F}_{ik,g_i\to g_j} \Rightarrow \\ \|\vec{F}_{g_i\to g_j}\left[\mathrm{N}\right]\| &= \sqrt{\sum_{u_r=x,y,z}\left(\sum_k \delta_{kj}\cdot\left|\vec{F}_{ik,g_i\to g_j}\cdot\vec{u}_r\right|\right)^2} \end{aligned} \tag{11}$$

where in Eq. (11):

- $\vec{u}_r[\mathrm{m}]$ is the unit vector for the r axis of the reference system

After some time δt, the boundary will have traveled an average dis-

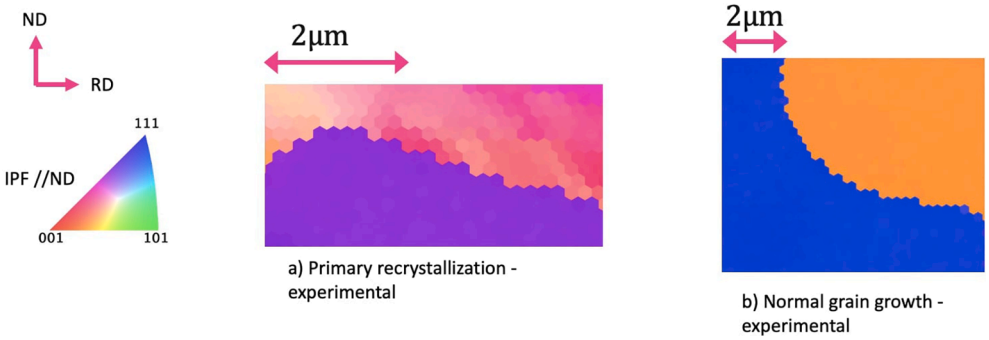

Fig. 2. EBSD observations during the annealing of the IF-steel sheet. The phenomena depicted are (a) primary recrystallization – i.e. a recrystallized grain grows into a substructure (b) grain growth - i.e. two recrystallized grains have impinged.

tance equal to $\|\vec{v}_{g_i\to g_j}\|\cdot\delta t$ and the force will have performed a work equal to the energy difference:

$$\|\vec{F}_{g_i\to g_j}\|\cdot\|\vec{v}_{g_i\to g_j}\|\cdot\delta t = \Delta E_{g_i\to g_j} \tag{12}$$

Defining then as $\dot{d}_{g_i\to g_j}$, the growth rate of g_j in cell i, we have:

$$\dot{d}_{g_i\to g_j} = 1\Big/\delta t \Rightarrow^{(4),(6),(7),(11),(12)} \dot{d}_{g_i\to g_j} = M_{g_i\to g_j}\cdot\sqrt{\sum_{u_r=x,y,z}\left(\sum_k \delta_{kj}\cdot\left|\vec{F}_{ik,g_i\to g_j}\cdot\vec{u}_r\right|\right)^2}\Big/V_i \tag{13}$$

2.4. Sharp-interface condition

A cell i re-orients to g_j with rate $\dot{d}^t_{g_i\to g_j}$ from Eq. (13) calculated at time t. After the incremental time δt the re-orientated fraction of cell i is:

$$f^{t+\delta t}_{g_i\to g_j} = \dot{d}^t_{g_i\to g_j}\cdot\delta t + f^t_{g_i\to g_j} \tag{14}$$

Cell i re-orients completely into g_j when $f^t_{g_i\to g_j}$ becomes equal to (or exceeds) the value of 1. The description of the algorithm's steps can be found in the Appendix.

3. Application

3.1. Input settings

3.1.1. Grid-related settings

The simulation is performed within a 2D automaton grid of hexagonal (regular hexagons) cells. Hence the parameters in the analytical expressions which relate to the grid are:

- $N = 6$ neighbours per cell
- $\vec{u}_{ji} \in \{\vec{u}_x, -\vec{u}_x, \cos(60^\circ)\cdot\vec{u}_x + \sin(60^\circ)\cdot\vec{u}_y, -\cos(60^\circ)\cdot\vec{u}_x + \sin(60^\circ)\cdot\vec{u}_y, -\cos(60^\circ)\cdot\vec{u}_x - \sin(60^\circ)\cdot\vec{u}_y, \cos(60^\circ)\cdot\vec{u}_x - \sin(60^\circ)\cdot\vec{u}_y\}$
- $A_{ij} = \delta x_{CA}\cdot|\vec{z}_{CA}|/(2\cdot\sqrt{0.75})\ \forall\ A_{ij} \neq 0$ where $\vec{z}_{CA}$ has direction perpendicular to the 2D grid and it is of arbitrary magnitude - it cancels out with $\vec{z}_{CA}$ from V_i once Eq. (6) and Eq. (4) are substituted in Eq. (13)
- $V_i = (3\cdot\sqrt{3}/2)(\delta x_{CA}/(\sqrt{0.75}\cdot 2))^2\cdot|\vec{z}_{CA}|\ \forall\ i$

In the above settings, $\vec{u}_x$ and $\vec{u}_y$ are the unit vectors of the (Cartesian) reference system.

3.1.2. Input material and microstructure

The chemical composition of the IF steel is shown in Table 2. The material parameters used are shown in Table 3 and the applied time–temperature profile is shown in Fig. 3.

The input RVE was obtained experimentally through high-resolution EBSD using a Sigma 500 microscope from Zeiss, coupled with OIM DC-software and a Hikari-Camera from EDAX. The crystal orientation at each cell of the automaton grid corresponded to the one measured for the pixel located at the same spatial coordinates. The spacing between adjacent hexagons δx_{CA} is equal to 0.12 μm and the number of cells comprising the RVE is 5316480.

The model's input is shown Fig. 4a. The maps in Fig. 4 are plotted with the use of PYEBSD [75]. In particular, the automaton cells are colored in accord with the IPF//ND and are darkened in ascending order with respect to the maximum misorientation from their neighbours. For example, if a cell has maximum misorientation from its neighbours less than 0.3° the cell is colored only in accord with the IPF//ND, while for larger misorientations the IPF coloring is darkened. Eventually a cell that is surrounded by at least one HAGB (i.e. $\theta_{ij} > 15^\circ$) appears black.

The substructure is shown more clearly in characteristic regions of the IF-steel sheet in Fig. 4b-d. In particular:

- Fig. 4b shows the substructure in the vicinity of a HAGB for the two deformed grains that are separated. The subgrains in these areas are coarse and the intergranular boundaries are generally of small misorientations – e.g. the boundaries marked by white arrows.
- Fig. 4c shows the substructure inside a grain where deformation bands have formed. As indicated by the dark color of the cells, the deformation bands are circumscribed by mostly large-angle boundaries. The subgrains (e.g. regions indicated by red arrows) are almost

Table 2
Chemical Composition – wt % of the IF steel used in the application.

C	Mn	Al	N	Ti	S	Cr
0.002	0.095	0.05	0.002	0.045	0.006	0.02

Table 3
Input parameters used in the simulation.

Quantity	Value	Description
Q_g	140 kJ/mol	activation energy for boundary migration from [72]
M_0	0.43 mol·m/Js	pre-exponential factor of HAGBs mobility
γ_{HAGB}	0.5 J/m^2	the energy per unit area of a HAGB from [73,74]
θ_{HAGB}	15°	minimum angle to consider a HAGB
θ_{min}	0.3°	minimum angle to consider the existence of a boundary between two neighbour CA cells
c	0.7	parameter used in Eq. (4)

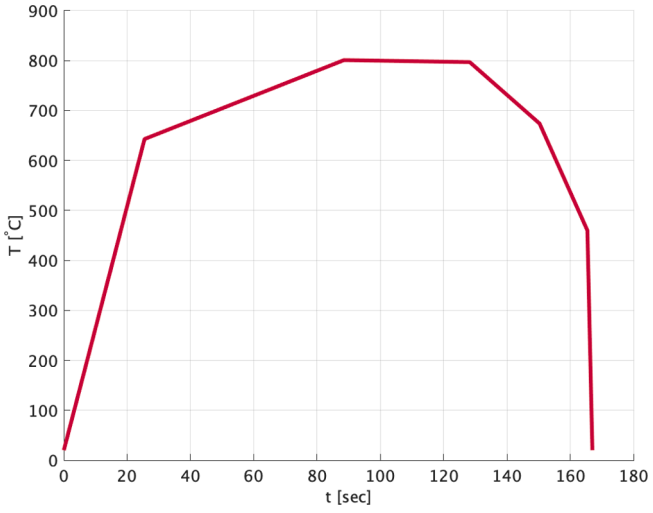

Fig. 3. The temperature-time profile applied to the sheet.

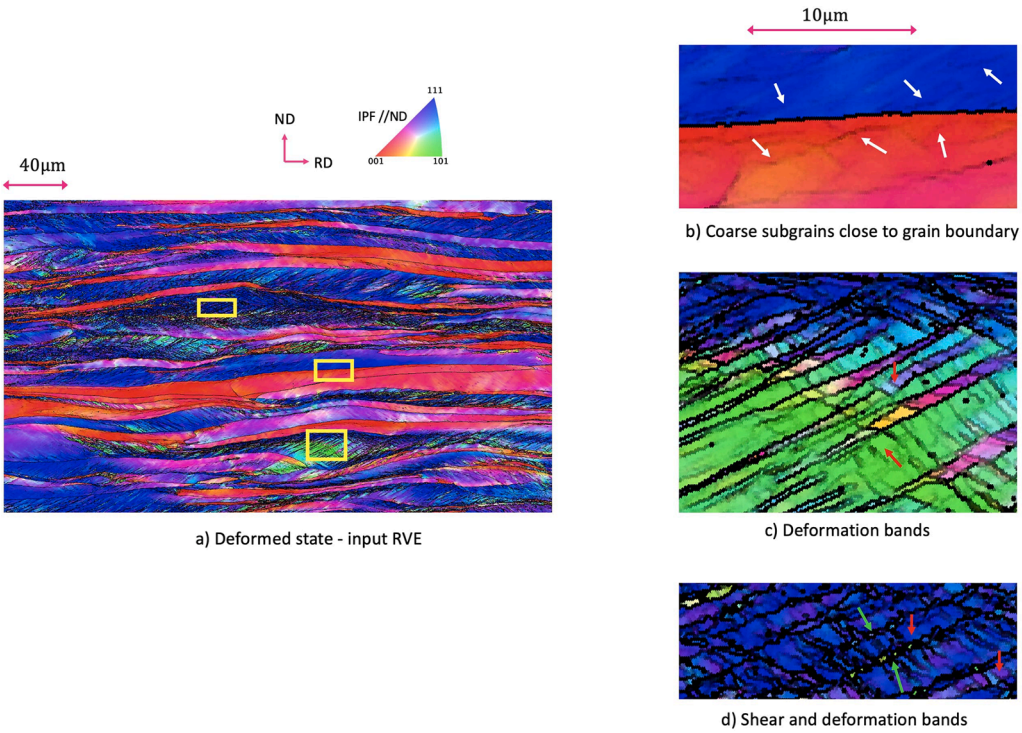

Fig. 4. Input RVE for the simulation: (a) the deformed state as imported in the CA (b) the substructure in the two opposite sides of a grain boundary (c) the substructure in deformation bands (d) the substructure in a region that includes shear and deformation bands.

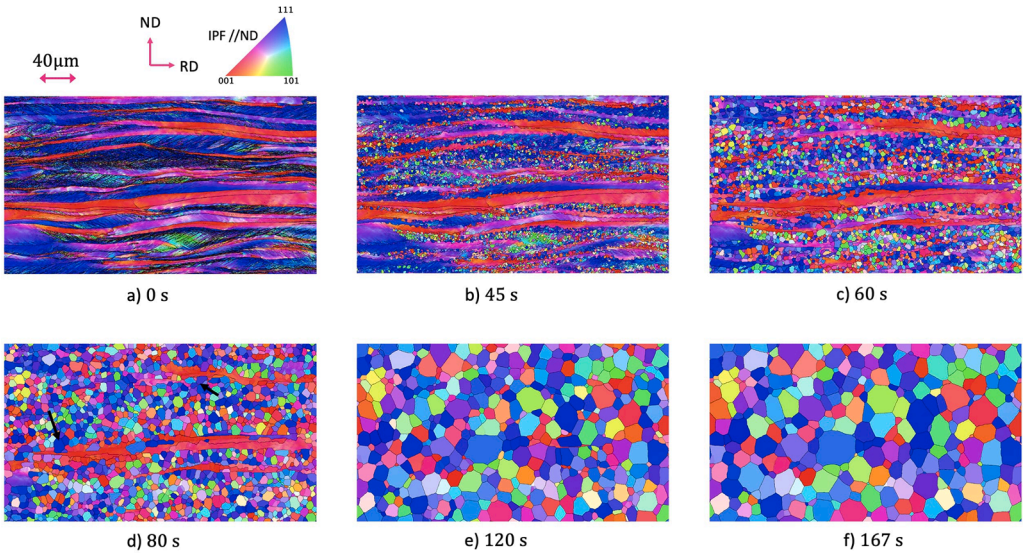

Fig. 5. Evolution of simulation at (a) 0 s (b) 45 s (c) 60 s (d) 80 s (e) 120 s and (f) 167 s.

rectangular and separated mostly by low-angle boundaries from adjacent subgrains within the same deformation band.

- Fig. 4d shows the substructure in an area where besides deformation bands, also shear bands can be distinguished (e.g. regions indicated by green arrows). Very high misorientation is found at the rims of shear bands where HAGBs have formed. Such bands enclose much smaller subgrains from the abutting matrix subgrains (e.g. see subgrains indicated by red arrows).

As shown in Fig. 4, many important topological characteristics of cold-rolled IF-steel sheets of similar thickness reductions are identified. Coarse subgrains with diffuse boundaries [5,67] as well as shear bands and deformation bands [1,5] are distinguished in the various regions that comprise the deformed metal. Additionally, the heterogeneity in the subgrain sizes and boundaries' misorientation is clear, throughout the RVE (e.g. between Fig. 4a and Fig. 4b) but also locally (e.g. the subgrains inside the narrow shear bands compared to their surroundings).

3.2. Simulated microstructure evolution

Fig. 5 shows the temporal evolution of the simulated microstructure. It is clear that already from the early stages of growth many CA cells have grown into the surrounding deformed matrix, yet in a spatially non-uniform fashion. For example at 45 s, some deformed grains have

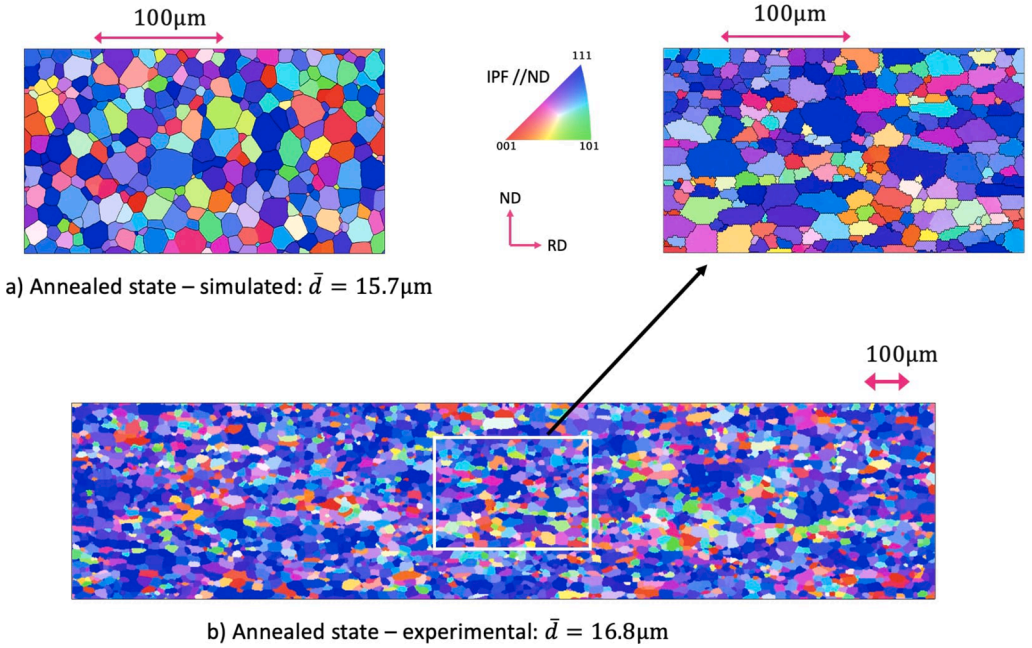

Fig. 6. Recrystallized cold-rolled IF steel; (a) the simulated microstructure (b) the experimental measurement.

already got partially consumed by strain-free volumes, while other less deformed regions (e.g. the reddish volume in Fig. 5b) have remained almost intact. Such deformed grains neither grow significantly nor get consumed by other recrystallized grains. This phenomenon has been confirmed by earlier experimental investigations in the evolution of recrystallization – e.g. in [76,77]. The resistance of low-stored energy deformed grains in recrystallising diminishes as grains in other regions nearby become eventually large enough (e.g. see the grains indicated by black arrows in Fig. 5d) to grow into them. Eventually, at the end of the simulation, all prior deformed grains have been replaced by equiaxed grains, within which dislocations are absent.

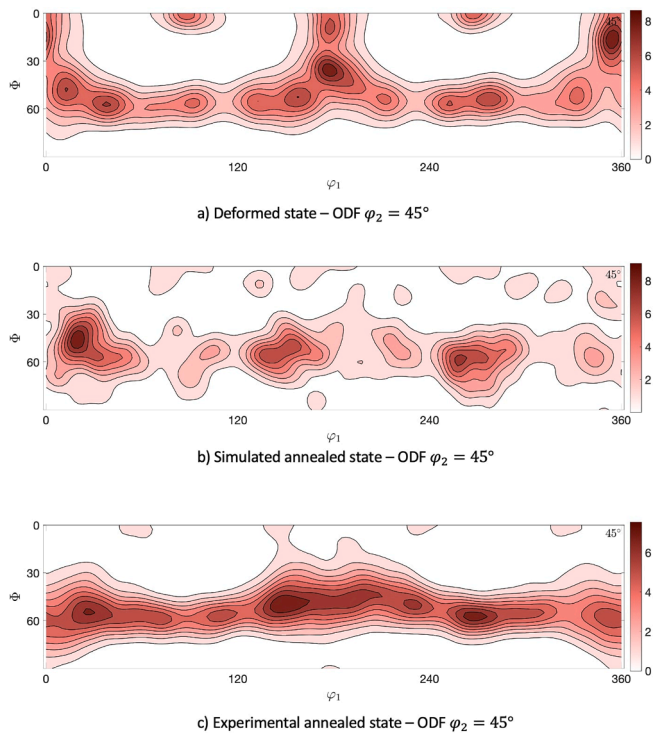

Fig. 7. ODF quantified and plotted in section $\phi_2 = 45°$ for (a) the deformed state (b) the simulated recrystallized microstructure (c) the experimental measurement of the annealed sheet.

3.3. Simulated and experimental relevance

Fig. 6 shows the annealed microstructure as simulated and measured experimentally, both corresponding to the temperature–time profile shown in Fig. 3. A Bähr DIL 805 A/D dilatometer was employed to perform the annealing treatment that resulted in the microstructure shown in Fig. 6b.

The average grain diameter was quantified after decomposing the orientation data into grains, using MTEX [78]. Although the average grain size is rather close between the simulated and the experimental microstructure – namely 15.7 μm and 16.8 μm, respectively, the grains' shape and size distribution do not seem to follow the experimentally measured microstructure's. In particular, the experimentally measured annealed state contains some considerably larger and pancake-shaped grains which are not observed in the simulated microstructure. This could be because the simulation was performed in 2D, whereas the (sub) grains' coarsening is a 3D phenomenon. In addition, differences in grains' shape and size distribution could result from variations in the particle pinning at HAGBs' which may exist [11,52,59–62], yet were not considered in the simulation.

Fig. 7 shows the $\phi_2 = 45°$ section of the orientation distribution function (ODF) for the deformed and annealed states. The ODFs were determined with the use of MTEX [78], by employing a 7° halfwidth. As shown in Fig. 7, while the deformed sheet is characterized by a combined α fiber (i.e. $\langle 110 \rangle // RD$) and γ fiber (i.e. $\langle 111 \rangle // ND$), the simulation results in the diminishing of α fiber components, while γ fiber components intensify. This is confirmed by the experimentally annealed sample (Fig. 7c) which is characterized by a full γ fiber texture. Although there are deviations between the experimental and the simulated annealed state, the texture components that comprise the simulated recrystallized microstructure are mostly located within the γ fiber. Therefore, the capillary competitive subgrain growth that is simulated has altered the distribution of relevant texture components, in compliance with the experimental findings.

Additionally, the change in the texture components' distribution that occurs upon the simulation indicates that the selective subgrain growth

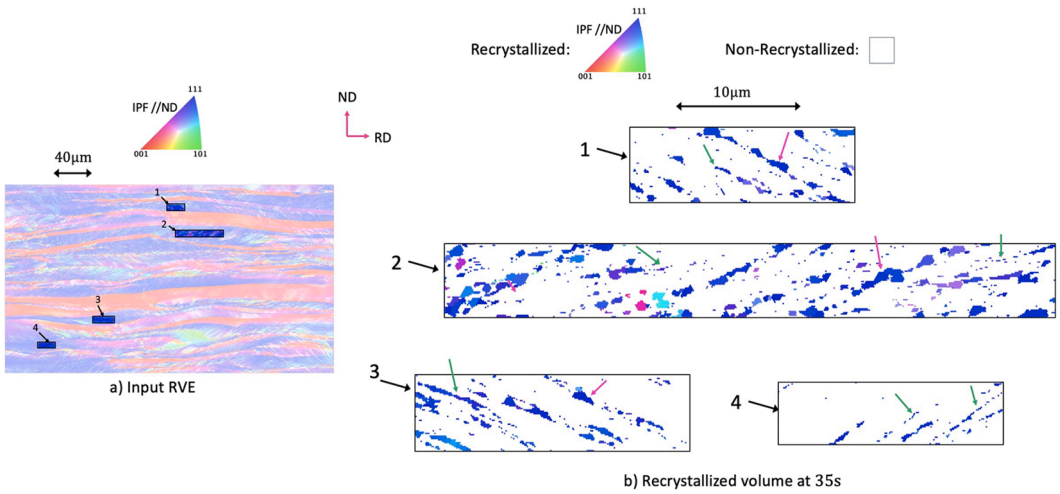

Fig. 8. Simulated results: early stages of recrystallization shown in grains where shear and deformation bands have formed (a) 0 s – the location of the areas studied is shown (b) 35 s - the volume which has been surpassed by a boundary (i.e. white color means that the cell has remained intact) is shown.

did not occur randomly. Instead, the topological characteristics important for recrystallization - e.g. the relationship (size, crystal orientations etc.) between a subgrain and its surroundings - follow an orientation-dependent pattern at the prior-deformed state.

3.4. Early stages of recrystallization

This section reviews the onset and evolution of recrystallization in specific characteristic areas of the sheet during the early stages of annealing.

3.4.1. Shear and deformation bands

Fig. 8 shows the early stages of recrystallization in various regions where shear and deformation bands are present. In Fig. 8a the locations of the areas investigated are shown and in Fig. 8b the recrystallized volume is shown at 35 s for the corresponding regions. More specifically, Fig. 8b shows the crystal direction//ND at 35 s for the cells which have been surpassed by a boundary, while the volume that has remained intact is plotted white. As shown in Fig. 8b, the recrystallized areas arrange along the axis of the prior shear or deformation bands. This phenomenon indicates that subgrains from the matrix (normally lower in stored deformation energy and thus larger) invade and consume the subgrains within the prior abutting shear or deformation bands [5,7].

Most of the recrystallized volume nonetheless stops expanding - e.g. the recrystallized volume indicated by green arrows in Fig. 8b which has not grown much or has grown only in the perpendicular direction of the prior bands. This is because the recrystallized volume met either similar crystal orientations or larger subgrains in the matrix [2]. Only some of the recrystallized grains continue to satisfy the two instability criteria, e.g. the ones indicated by pink arrows in Fig. 8b.

As an example, the boundaries' temporal evolution in region 3 (shown in Fig. 8b) is illustrated in Fig. 9. As shown in Fig. 9, recrystallization initiates through HAGBs that surround deformation bands. However, many of the pre-existing HAGBs (e.g. B1-B4 indicated by pink arrows in Fig. 9) become low-angle boundaries after surpassing the narrow deformation band. This is understood by the color of boundaries B1-B4, which changes from black (see Fig. 9a) to gray (see Fig. 9c).

3.4.2. Competitive growth at different HAGBs

Figs. 10 and 11 show the competitive growth that takes place at characteristic regions of the deformed state where different types of HAGBs are present. Fig. 10 shows a grain characterized by low-stored energy (grain A) in contact with a grain within which shear and deformation bands have formed (grain B). Fig. 11 shows a grain with low-stored energy (grain C) abutting a grain where shear/deformation bands have formed in two directions and thus intersect (grain D). The latter is identified by the consideration of both Fig. 11a and Fig. 11b. In particular, one group of bands incorporates orientation gradients mostly along the ND while in the other group these are found along the RD. Concerning the recrystallization evolution, the following is observed:

- Inside grains with low deformation: Within grains A and C in Figs. 10 and 11 there is complete absence of recrystallization. This is due to the lack of sufficiently high intergranular orientation gradients resulting in such deformed regions remaining intact.
- Pre-existing subgrains next to conventional grain boundaries: Only a small portion of the deformed matrix in contact with conventional grain boundaries - the boundaries between grains A-B and C-D - has recrystallized. Although subgrains abutting conventional grain boundaries have a kinetic advantage and are also in general large,

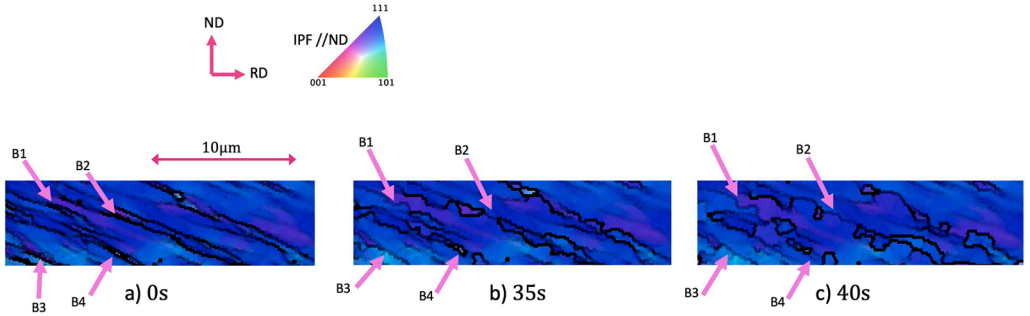

Fig. 9. Simulated results: temporal evolution in the early stages of recrystallization at deformation bands (a) 0 s (b) 35 s (c) 40 s.

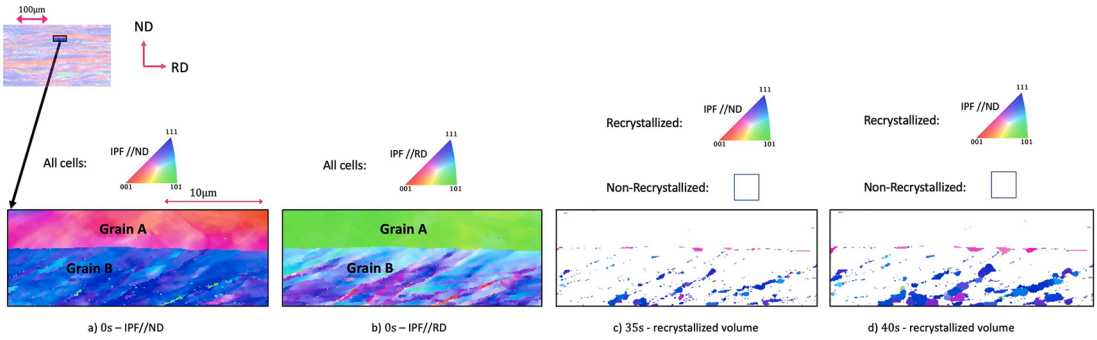

Fig. 10. Simulated results: early stages of recrystallization shown in an area consisting of two deformed grains at (a) 0 s – IPF//ND (b) 0 s - IPF//RD (c) 35 s – the volume which has been surpassed by a boundary is color-coded with IPF//ND (d) 40 s - the volume which has been surpassed by a boundary is color-coded with IPF//ND.

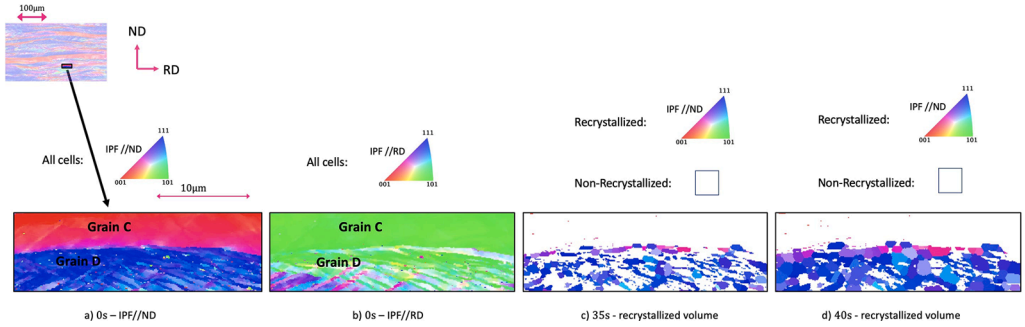

Fig. 11. Simulated results: early stages of recrystallization shown in an area consisting of two deformed grains at (a) 0 s – IPF//ND (b) 0 s – IPF//RD (c) 35 s – the volume which has been surpassed by a boundary is color-coded with IPF//ND (d) 40 s – the volume which has been surpassed by a boundary is color-coded with IPF//ND.

their growth does not produce large recrystallized volumes. It is then clear that such subgrains in general do not have a size advantage. This was also shown in Fig. 4, where no significant differences in the subgrain sizes or misorientations were observed between the two sides close to the grain boundary. Hence, a subgrain in the vicinity of a grain boundary may start bulging in the adjacent deformed matrix, but it is very likely that the motion will stop because larger subgrains will be met.

- Inside grains with bands of one direction: Recrystallization occurs in grain B in a fashion similar to the evolution presented in Fig. 8. The pre-existing subgrains adjacent to the narrow deformation bands have grown at the expense of the smaller subgrains within them.
- Inside grains with intersecting shear and deformation bands: Recrystallization predominates in grain D. Comparing for example the evolution of recrystallization in grain B to grain D, from Figs. 10 and 11 respectively, it seems that recrystallization is favored when shear/deformation bands in two different directions intersect. This can be explained if one considers that in such a region (grain D) after surpassing the first shear/deformation band, the bulged volume will not meet the same crystal orientation. Additionally, when orientation gradients are present in two different directions, the recrystallization front can grow in both and thereby provide a size advantage to the recrystallized volume.

4. Conclusions

A curvature-driven algorithm was applied to a Ti-stabilized IF steel cold-rolled up to 77% thickness reduction. The following remarks can be deduced from the recrystallization simulations:

- Although recrystallization nucleation is not artificially imposed in the present modeling framework, it occurs upon the simulation due to the highly heterogeneous subgrain coarsening that takes place in the early stages of annealing. Followed by the subsequent growth of the recrystallized grains, the simulation yields a fully recrystallized microstructure.
- In compliance with the experimental observations, the simulation results in the diminishing of texture components within the ⟨110⟩// RD fiber while mostly texture components within the ⟨111⟩//ND fiber comprise the recrystallized state. This indicates that in the as-deformed state, the presence of subgrains in a favorable location to recrystallize – such that they have a size and kinetic advantage - is an orientation-dependent phenomenon.
- Recrystallization at shear and deformation bands occurs primarily by the invasion of matrix subgrains in the substructure within the adjacent narrower bands. However, in most cases, the recrystallized volume stops expanding once surpassing the first shear/deformation band, because the boundaries are no longer high-angle.
- Subgrains growing in regions with intersecting shear/deformation bands become very soon distinguished in their size compared to subgrains within regions where all the narrow bands are parallel.
- A subgrain's likelihood to recrystallize depends on its surroundings in the following order: subgrains next to intersecting shear bands, subgrains next to shear bands arranged in one direction, subgrains next to conventional grain boundaries.

Data availability

The experimental measurements and the simulated microstructures required to reproduce these findings are available to download from https://data.mendeley.com/datasets/6467hnvfpn/draft?a=77216290-d309-44bd-8fdb-b0c143bda53a. The algorithm required to reproduce the simulations cannot be shared at this time due to legal or ethical reasons.

CRediT authorship contribution statement

Konstantina Traka: Conceptualization, Methodology, Software, Validation, Formal analysis, Investigation, Writing - original draft, Visualization. **Karo Sedighiani:** Visualization, Investigation, Validation, Writing - original draft. **Cornelis Bos:** Writing - review & editing, Resources, Software. **Jesus Galan Lopez:** Investigation, Writing - review & editing, Resources, Software. **Katja Angenendt:** Investigation, Resources, Data curation. **Dierk Raabe:** Resources, Writing - review & editing, Supervision, Project administration, Funding acquisition. **Jilt Sietsma:** Resources, Writing - review & editing, Supervision, Project administration, Funding acquisition.

Declaration of competing interest

The authors declare that they have no known competing financial interests or personal relationships that could have appeared to influence the work reported in this paper.

Acknowledgements

This research was carried out under the project number S41.5.15572b in the framework of the Partnership Program of the Materials Innovation Institute M2i (www.m2i.nl) and the Technology Foundation STW (www.stw.nl), which is part of the Netherlands Organization for Scientific Research (www.nwo.nl). Particularly the authors would like to thank Vitesh Shah, Anthony Rollett, Martin Diehl, Konstantinos Kouzoumis, Leo Kestens, Erik Offerman, Winfried Kranendonk, and Pablo Garcia Chao for the very insightful and interesting discussions.

Appendix A

A.1. Algorithm's steps

At the initial state, the automaton identifies the orientation of every cell as a unique property. Every interfacial cell i (cell of at least one neighbour differently oriented i.e. $\exists\ j:\ A_{ij} \neq 0\ \Lambda\ \delta_{ij} = 0$ where δ_{ij} is defined in Eq. (2)) is stored at every time step. In a certain time step the algorithm performs the following:

- Step 1: A loop initiates for all the cells which are defined as interfacial cells.
- Step 2: For the i interfacial cell a loop initiates on its 1st Von-Neumann neighbours. The misorientation is calculated and stored for every pair of cells i and j. By using then Eq. (3) the value of $\gamma(g_i, g_j)$ is found and $\gamma(g_i, g_j)\cdot A_{ij}$ is added to the current state's energy (of cell i). A second loop initiates for each neighbour k among the 1st Von-Neumann neighbours of i (again). This is to calculate the misorientation between j and the rest k cells which are neighbours of i, and it will be used later. At the end of the double loop, cell's i energy (second term in Eq. (4)) and the misorientation inbetween all 1st Von-Neumann neighbour of i have been calculated.
- Step 3: For the same i interfacial cell the 1st Von-Neumann neighbours of the cell are looped again - now as candidates to re-orient i. The direction of boundary migration i.e. $\vec{u}_{ji}$ for every j cell is stored also here for the possible re-orientation of i into g_j. Inside this loop, the 1st Von-Neumann neighbours of i are looped once more to calculate the next state's energy for every candidate re-orientation (with the use of the calculated misorientations from step 2, and Eq. (3)) by assuming the next state's boundaries i.e. between i and k where i is supposed to be orientated as j. If cell k is similarly oriented with j (i.e. $\delta_{jk} = 1$ in Eq. (2)) then the direction of growth i.e. $\vec{u}_{ki}$ for the k cell is stored since k will grow together with cell j. Then the loop continues since a boundary between i and k will not exist if i re-orients as g_j. If not, then first the cell l is considered, which is found from equating the position vectors $\vec{ji} = \vec{lk}$. Eq. (5) is then applied for the combination of cells i, j, k, l - i.e. if cell l is similarly oriented with j (which is growing into i) and can grow into cell k in the same direction as j will grow into i. If this l cell is found eligible to grow into k (i.e. $\delta_{lkij} = 1$ in Eq. (5)) then the boundary energy between k and i, after the latter re-orients into g_j is added in the next state's energy as $(1-c)\cdot\gamma(g_j, g_k)\cdot A_{ik}$. If l is not eligible, then the boundary energy is added as $\gamma(g_j, g_k)\cdot A_{ik}$. This loop continues in the same way for all k cells. At the end of this loop, the next state's energy for j cell growing into i is calculated and substituted in Eq. (4) together with the current state's energy for i cell which was calculated in step 2. If the energy change is positive then the re-orientation rate is found (see Eq. (13)) for cell i re-orienting as j, by using Eq. (9), Eq. (8) and the (already) calculated Eq. (4), and $\vec{u}_r, \vec{u}_{ki}\ \forall\ k:\ \delta_{jk} = 1$ including $k = j$ (as mentioned the position vectors $\vec{u}_{ki}$ were stored). If the re-orientation rate of i into g_j is positive and larger than any other re-orientation rate for i cell then the re-orientation rate is stored together with the orientation g_j for the i cell.
- Step 4: Step 3 is done for all j cells that are candidates to re-orient cell i and at the end one (the faster) re-orientation rate $\dot{d}_{g_i \to g_j}$ for cell i (if any) is kept along with g_j.
- Step 5: Steps 2–4 are performed for every i interfacial cell. After all i cells are looped and their re-orientation rate is defined the maximum re-orientation rate $\dot{d}_{max}$ at the current time step is also found. The time step's (i.e. incremental simulation time) value is found as $\delta t = 1/\dot{d}_{max}$, for the particular time of the simulation.
- Step 6: The time step δt is added to the simulation's time and then every cell i is looped to apply the new re-orientation fraction given in Eq. (14). If a cell i has re-orientation fraction larger or equal to 1 it transforms (i.e. re-orients) to the favorable orientation and the re-orientation fraction is set back to zero. The cell i - now oriented as g_j - is then stored in order to recalculate the relevant interfacial cells.
- Step 7: The neighbours of every i cell that re-oriented at the current time step are found and added to the structure of interfacial cells. The procedure from step 1 starts again.

References

[1] W.B. Hutchinson, Development and control of annealing textures in low-carbon steels, Int. Metals Rev. 29 (1) (1984) 25–42, https://doi.org/10.1179/imtr.1984.29.1.25. ISSN 0308-4590.

[2] Bevis Hutchinson, Nucleation of recrystallisation, Scr. Metall. Mater. 27 (11) (1992) 1471–1475, https://doi.org/10.1016/0956-716X(92)90130-7. ISSN 0956716X.

[3] Kyoo Young Lee, Gyo Sung Kim, Kwang Geun Chin, Leo Kestens, The evolution of texture and stored energy during recrystallization of if high strength steel investigated by means of orientation imaging microscopy, Mater. Sci. Forum

558–559 (2007) 241–246, https://doi.org/10.4028/www.scientific.net/MSF.558-559.241. ISSN 1662-9752.
[4] D. Raabe, On the orientation dependence of static recovery in low-carbon steels, Scr. Metall. Mater. 33 (5) (1995) 735–740, https://doi.org/10.1016/0956-716X(95)00276-2. ISSN 0956716X.
[5] Dierk Raabe, Recovery and recrystallization: phenomena, physics, models, simulation, in: Physical Metallurgy, pages 2291–2397. Elsevier, 2014. ISBN 978-0-444-53770-6.
[6] Kohsaku Ushioda, Advances in research on deformation and recrystallization for the development of high-functional steels. Sci. Technol. Adv. Mater., 21 (1): 29–42, January 2020. 1878–5514. ISSN 1468-6996 doi: 10.1080/14686996.2019.1710013.
[7] Kohsaku Ushioda, W.B. Hutchinson, Role of shear bands in annealing texture formation in 3%Si-Fe(111)[112] single crystals, ISIJ Int. 29 (10) (1989) 862–867, https://doi.org/10.2355/isijinternational.29.862. ISSN 0915-1559.
[8] Y. Inokuti, R.D. Doherty, Transmission kossel study of the structure of cold-rolled iron and its nucleation behaviour, Text. Crystal. Solids 2 (3) (1977) 143–168, https://doi.org/10.1155/TSM.2.143. ISSN 0309-7951.
[9] Y. Inokuti, R.D. Doherty, Transmission kossel study of the structure of compressed iron and its recrystallization behaviour, Acta Metall. 26 (1) (1978) 61–80, https://doi.org/10.1016/0001-6160(78)90202-X. ISSN 00016160.
[10] G. Ibe and K. Lücke, Über die spontane Keimbildung bei der Herstellung von Einkristallen durch Rekristallisation. Kristall und Technik, 2 (2): 177–190, 1967. ISSN 00234753 15214079. doi: 10.1002/crat.19670020204.
[11] K. Verbeken, L. Kestens, M.D. Nave, Re-evaluation of the Ibe-Lücke growth selection experiment in a Fe-Si single crystal, Acta Mater. 53 (9) (2005) 2675–2682, https://doi.org/10.1016/j.actamat.2005.02.030. ISSN 13596454.
[12] B.J. Duggan, Y.Y. Tse, G. Lam, and M.Z. Quadir. Deformation and Recrystallization of Interstitial Free (IF) Steel. Mater. Manuf. Process., 26 (1): 51–57, February 2011. ISSN 1042-6914 1532–2475. doi: 10.1080/10426910903202237.
[13] R.D. Doherty, D.A. Hughes, F.J. Humphreys, J.J. Jonas, D. Juul Jensen, M. E. Kassner, W.E. King, T.R. McNelley, H.J. McQueen, A.D. Rollett, Current issues in recrystallization: a review, Mater. Sci. Eng.: A 238 (2) (1997) 219–274, https://doi.org/10.1016/S0921-5093(97)00424-3. ISSN 09215093.
[14] Roger D. Doherty, Recrystallization and texture, Prog. Mater Sci. 42 (1–4) (1997) 39–58, https://doi.org/10.1016/S0079-6425(97)00007-8. ISSN 00796425.
[15] Miho Tomita, Tooru Inaguma, Hiroaki Sakamoto, and Kohsaku Ushioda, Recrystallization behavior and texture evolution in severely cold-rolled Fe-0.3mass %Si and Fe-0.3mass%Al alloys. ISIJ Int., 57 (5): 921–928, 2017. ISSN 0915-1559 1347–5460. doi: 10.2355/isijinternational.ISIJINT-2016-634.
[16] S. Dziaszyk, E.J. Payton, F. Friedel, V. Marx, G. Eggeler, On the characterization of recrystallized fraction using electron backscatter diffraction: A direct comparison to local hardness in an IF steel using nanoindentation, Mater. Sci. Eng.: A 527 (29–30) (2010) 7854–7864, https://doi.org/10.1016/j.msea.2010.08.063. ISSN 09215093.
[17] Rajesh Khatirkar, Basavaraj Vadavadagi, Arunansu Haldar, and Indradev Samajdar, ND recrystallization in interstitial free steel: the defining role of growth inhibition, ISIJ Int., 52 (5): 894–901, 2012. ISSN 0915-1559 1347–5460. doi: 10.2355/isijinternational.52.894.
[18] A. Ayad, M. Ramoul, A.D. Rollett, F. Wagner, Quantifying primary recrystallization from EBSD maps of partially recrystallized states of an IF steel, Mater. Charact. 171 (2021), 110773, https://doi.org/10.1016/j.matchar.2020.110773. ISSN 10445803.
[19] Dong-Kyu Kim, Wanchuck Woo, Won-Woong Park, Yong-Taek Im, Anthony Rollett, Mesoscopic coupled modeling of texture formation during recrystallization considering stored energy decomposition, Comput. Mater. Sci. 129 (2017) 55–65, https://doi.org/10.1016/j.commatsci.2016.11.048. ISSN 09270256.
[20] A.D. Rollett, Crystallographic texture change during grain growth. JOM, 56 (4): 63–68, April 2004. 1543–1851. ISSN 1047-4838 doi: 10.1007/s11837-004-0075-9.
[21] A.D. Rollett, D. Raabe, A hybrid model for mesoscopic simulation of recrystallization, Comput. Mater. Sci. 21 (1) (2001) 69–78, https://doi.org/10.1016/S0927-0256(00)00216-0. ISSN 09270256.
[22] S.-H. Choi, F. Barlat, J.H. Chung, Modeling of textures and yield surfaces during recrystallization in IF steel sheets, Scripta Mater. 45 (10) (2001) 1155–1162, https://doi.org/10.1016/S1359-6462(01)01133-2. ISSN 13596462.
[23] Shi-Hoon Choi and Jae Hyung Cho, Primary recrystallization modelling for interstitial free steels, Mater. Sci. Eng.: A 405 (1–2) (2005) 86–101, https://doi.org/10.1016/j.msea.2005.05.093. ISSN 09215093.
[24] Dierk Raabe and Richard C Becker, Coupling of a crystal plasticity finite-element model with a probabilistic cellular automaton for simulating primary static recrystallization in aluminium. Modell. Simul. Mater. Sci. Eng., 8 (4): 445–462, July 2000. ISSN 0965-0393 1361–651X. doi: 10.1088/0965-0393/8/4/304.
[25] Dierk Raabe, Luc Hantcherli, 2D cellular automaton simulation of the recrystallization texture of an IF sheet steel under consideration of Zener pinning, Comput. Mater. Sci. 34 (4) (2005) 299–313, https://doi.org/10.1016/j.commatsci.2004.12.067. ISSN 09270256.
[26] Shiun Ling and Michael P. Anderson, Monte Carlo simulation of grain growth and recrystallization in polycrystalline materials. JOM, 44 (9): 30–36, September 1992. ISSN 1047-4838 1543–1851. doi: 10.1007/BF03222323.
[27] T. Takaki, A. Yamanaka, Y. Higa, and Y. Tomita, Phase-field model during static recrystallization based on crystal-plasticity theory, J. Comput.-Aid. Mater. Des., 14 (S1): 75–84, December 2007. ISSN 0928-1045 1573–4900. doi: 10.1007/s10820-007-9083-8.
[28] Håkan Hallberg, Frédéric Adamski, Sarah Baïz, and Olivier Castelnau, Microstructure and property modifications of cold rolled IF steel by local laser annealing. Metall. Mater. Trans. A, 48 (10): 4786–4802, October 2017. ISSN 1073-5623 1543–1940. doi: 10.1007/s11661-017-4210-y.
[29] Paul A. Beck, The formation of recrystallization nuclei. J. Appl. Phys., 20 (6): 633–634, June 1949. ISSN 0021-8979 1089–7550. doi: 10.1063/1.1698446.
[30] A.H. Cottrell, Theory of dislocations, Progr. Metal Phys. 4 (1953) 205–264, https://doi.org/10.1016/0502-8205(53)90018-5. ISSN 05028205.
[31] Paulo Rangel Rios, Fulvio Siciliano Jr, Hugo Ricardo Zschommler Sandim, Ronald Lesley Plaut, and Angelo Fernando Padilha, Nucleation and growth during recrystallization. Mater. Res., 8 (3): 225–238, September 2005. ISSN 1516-1439. doi: 10.1590/S1516-14392005000300002.
[32] Paul A. Beck, Philip R. Sperry, and Hsun Hu, The orientation dependence of the rate of grain boundary migration. J. Appl. Phys., 21 (5): 420–425, May 1950. ISSN 0021-8979 1089–7550. doi: 10.1063/1.1699676.
[33] A.D. Rollett and E.A. Holm, Abnormal grain growth – The origin of recrystallization nuclei? Technical Report SAND–97-1712C, CONF-9610242–6, 527513, August 1997.
[34] R.W. Cahn, Recrystallization of single crystals after plastic bending, J. Inst. Metals 76 (2) (1949) 121.
[35] R.W. Cahn, Internal strains and recrystallization, Progr. Metal Phys. 2 (1950) 151–176, https://doi.org/10.1016/0502-8205(50)90008-6. ISSN 05028205.
[36] R W Cahn, A new theory of recrystallization nuclei. Proc. Phys. Soc. Sect. A, 63 (4): 323–336, April 1950. ISSN 0370-1298. doi: 10.1088/0370-1298/63/4/302.
[37] Fengbo Han, Bin Tang, Hongchao Kou, Jinshan Li, and Yong Feng, Cellular automata modeling of static recrystallization based on the curvature driven subgrain growth mechanism. J. Mater. Sci., 48 (20): 7142–7152, October 2013. ISSN 0022-2461 1573–4803. doi: 10.1007/s10853-013-7530-3.
[38] F.J. Humphreys, A unified theory of recovery, recrystallization and grain growth, based on the stability and growth of cellular microstructures–I. The basic model, Acta Mater. 45 (10) (1997) 4231–4240.
[39] F.J. Humphreys, Gregory S. Rohrer, and Anthony D. Rollett, Recrystallization and related annealing phenomena. Elsevier, Amsterdam Oxford Cambridge, MA, third edition, 2017. ISBN 978-0-08-098269-4 978-0-08-098235-9.
[40] P. Faivre and R.D. Doherty, Nucleation of recrystallization in compressed aluminium: studies by electron microscopy and Kikuchi diffraction. J. Mater. Sci., 14 (4): 897–919, April 1979. ISSN 0022-2461 1573–4803. doi: 10.1007/BF00550722.
[41] Choh Hsien Li, E.H Edwards, J Washburn, and E.R Parker. Stress-induced movement of crystal boundaries. Acta Metall., 1 (2): 223–229, March 1953. ISSN 00016160 doi: 10.1016/0001-6160(53)90062-5.
[42] M Winning, G Gottstein, and L S Shvindlerman, On the mechanisms of grain boundary migration. Acta Mater., page 11, 2002.
[43] Md. Kashif Rehman and Hatem S. Zurob, A novel approach to model static recrystallization of austenite during hot rolling of Nb Microalloyed steel. Part I: precipitate-free case. Metall. Mater. Trans. A, 44 (4): 1862–1871, April 2013. ISSN 1073-5623 1543–1940. doi: 10.1007/s11661-012-1526-5.
[44] Fengbo Han, Bin Tang, Hongchao Kou, Liang Cheng, Jinshan Li, and Yong Feng, Static recrystallization simulations by coupling cellular automata and crystal plasticity finite element method using a physically based model for nucleation. J. Mater. Sci., 49 (8): 3253–3267, April 2014. ISSN 0022-2461 1573–4803. doi: 10.1007/s10853-014-8031-8.
[45] Bevis Hutchinson, Deformation microstructures and textures in steels. Phil. Trans. R. Soc. Lond. Ser. A: Math., Phys. Eng. Sci., 357 (1756): ISSN 1471-2962 1471–1485, June 1999. doi: 10.1098/rsta.1999.0385.
[46] M.F. Ashby, The deformation of plastically non-homogeneous materials, Phil. Mag.: J. Theor. Exp. Appl. Phys. 21 (170) (1970) 399–424, https://doi.org/10.1080/14786437008238426. ISSN 0031-8086.
[47] Seong-Hee Lee, Hiroshi Utsunomiya, and Tetsuo Sakai, Microstructures and mechanical properties of ultra low carbon interstitial free steel severely deformed by a multi-stack accumulative roll bonding process. Mater. Trans., 45 (7): ISSN 1345-9678 2177–2181, 2004. 1347–5320. doi: 10.2320/matertrans.45.2177.
[48] Saeed Tamimi, Jose J. Gracio, Augusto B. Lopes, Said Ahzi, Frederic Barlat, Asymmetric rolling of interstitial free steel sheets: Microstructural evolution and mechanical properties, J. Manuf. Process. 31 (2018) 583–592, https://doi.org/10.1016/j.jmapro.2017.12.014. ISSN 15266125.
[49] D. Shan and L. Zhen, Aging behavior and microstructure evolution in the processing of aluminum alloys. In Microstructure Evolution in Metal Forming Processes, pages 267–297. Elsevier, 2012. ISBN 978-0-85709-074-4. doi: 10.1533/9780857096340.3.267.
[51] R.D. Doherty, R.W. Cahn, Nucleation of new grains in recrystallization of cold-worked metals, J. Less Common Metals 28 (2) (1972) 279–296, https://doi.org/10.1016/0022-5088(72)90131-2. ISSN 00225088.
[52] G. Gottstein and L.S. Shvindlerman, Grain boundary migration in metals: thermodynamics, kinetics, applications. CRC series in materials science and technology. Taylor & Francis, Boca Raton, 2nd ed edition, 2010. ISBN 978-1-4200-5435-4. OCLC: ocn166358378.
[53] A.D. Rollett, G. Gottstein, L.S. Shvindlerman, D.A. Molodov, Grain boundary mobility - a brief review, Z. Metall. 95 (4) (2004) 226–229, https://doi.org/10.3139/146.017938. ISSN 0044-3093.
[54] M. Upmanyu, R.W. Smith, D.J. Srolovitz, Atomistic simulation of curvature driven grain boundary migration, Interface Sci. 6 (1/2) (1998) 41–58, https://doi.org/10.1023/A:1008608418845. ISSN 09277056.
[55] Arunansu Haldar, Satyam Suwas, and Debashish Bhattacharjee, editors. Microstructure and Texture in Steels. Springer London, London, 2009. ISBN 978-1-84882-453-9 978-1-84882-454-6. doi: 10.1007/978-1-84882-454-6.

[56] Xiao Li, Ping Yang, Li Meng, Formation of the 111 and 111 recrystallization texture in deep drawing low carbon steel, Adv. Mater. Res. 535–537 (2012) 687–691, https://doi.org/10.4028/www.scientific.net/AMR.535-537.687. ISSN 1662-8985.
[57] R.L. Every, M. Hatherly, Oriented nucleation in low-carbon steels, Texture 1 (3) (1974) 183–194, https://doi.org/10.1155/TSM.1.183. ISSN 0371-6554.
[58] L.A.I. Kestens and H. Pirgazi, Texture formation in metal alloys with cubic crystal structures. Mater. Sci. Technol., 32 (13): 1303–1315, ISSN 0267-0836, 1743-2847. September 2016. 1743–2847. doi: 10.1080/02670836.2016.1231746.
[59] G. Ibe, K. Lücke, Arch. Eisenhiittenwes. 39 (1968) 693.
[60] Martin Hölscher, Dierk Raabe, Kurt Lücke, Rolling and recrystallization textures of bcc steels, Steel Res. 62 (12) (1991) 567–575, https://doi.org/10.1002/srin.199100451. ISSN 01774832.
[61] Kaneharu Okuda and Kazuhiro Seto, Recrystallization of isolated deformed grains in high purity iron. ISIJ Int., 55 (4): 877–883, 2015. 1347–5460. ISSN 0915-1559, doi: 10.2355/isijinternational.55.877.
[62] R.K. Ray, J.J. Jonas, and R.E. Hook, Cold rolling and annealing textures in low carbon and extra low carbon steels. Int. Mater. Rev., 39 (4): 129–172, January 1994. 1743–2804. ISSN 0950-6608, doi: 10.1179/imr.1994.39.4.129.
[63] C. Bos, M.G. Mecozzi, J. Sietsma, A microstructure model for recrystallisation and phase transformation during the dual-phase steel annealing cycle, Comput. Mater. Sci. 48 (3) (2010) 692–699, https://doi.org/10.1016/j.commatsci.2010.03.010. ISSN 09270256.
[64] C. Bos, M.G. Mecozzi, D.N. Hanlon, M.P. Aarnts, and J. Sietsma, Application of a three-dimensional microstructure evolution model to identify key process settings for the production of dual-phase steels. Metall. Mater. Trans. A, 42 (12): 3602–3610, December 2011. ISSN 1073-5623, 1543–1940. doi: 10.1007/s11661-011-0696-x.
[65] Dierk Raabe, Cellular automata in materials science with particular reference to recrystallization simulation. Annu. Rev. Mater. Res., 32 (1): 53–76, August 2002. 1545–4118.ISSN 1531-7331, 1543-1940 doi: 10.1146/annurev.matsci.32.090601.152855.
[66] I.L. Dillamore, C.J.E. Smith, T.W. Watson, Oriented nucleation in the formation of annealing textures in iron, Metal Sci. J. 1 (1) (1967) 49–54, https://doi.org/10.1179/msc.1967.1.1.49. ISSN 0026-0681.
[67] I. Thomas, S. Zaefferer, F. Friedel, and D. Raabe, High-Resolution EBSD Investigation of deformed and partially Recrystallized IF steel. Adv. Eng. Mater., 5 (8): 566–570, August 2003. 1527–2648. ISSN 1438-1656 doi: 10.1002/adem.200300373.
[68] A Martínez-de Guerenu, F Arizti, M Díaz-Fuentes, and I Gutérrez, Recovery during annealing in a cold rolled low carbon steel. Part I: Kinetics and microstructural characterization. Acta Mater., 52 (12): 3657–3664, July 2004. ISSN 13596454. doi: 10.1016/j.actamat.2004.04.019.
[69] J.G. Kemeny, Theory of self-reproducing automata. John von Neumann. Edited by Arthur W. Burks. University of Illinois Press, Urbana, 1966. 408 pp., illus. $10. Science, 157 (3785): 180–180, July 1967. ISSN 0036-8075 1095-9203. doi: 10.1126/science.157.3785.180.
[70] W.T. Read, W. Shockley, Dislocation models of crystal grain boundaries, Phys. Rev. 78 (3) (1950) 275–289, https://doi.org/10.1103/PhysRev.78.275. ISSN 0031-899X.
[71] David Turnbull, Theory of grain boundary migration rates. JOM, 3 (8): 661–665, August 1951. ISSN 1047-4838 1543–1851. doi: 10.1007/BF03397362.
[72] M. Hillert, L. Hoglund, Mobility of a/? phase interfaces in Fe alloys, Scripta Mater. 54 (7) (2006) 1259–1263, https://doi.org/10.1016/j.scriptamat.2005.12.023. ISSN 13596462.
[73] C. Hutchinson, H. Zurob, C. Sinclair, Y. Brechet, The comparative effectiveness of Nb solute and NbC precipitates at impeding grain-boundary motion in Nb steels, Scripta Mater. 59 (6) (2008) 635–637, https://doi.org/10.1016/j.scriptamat.2008.05.036. ISSN 13596462.
[74] Vitesh Shah, Monika Krugla, Sven Erik Offerman, Jilt Sietsma, and David Neal Hanlon. Effect of silicon, manganese and heating rate on the ferrite recrystallization kinetics. ISIJ Int., 60 (6): 1312–1323, June 2020. ISSN 0915-1559 1347–5460. doi: 10.2355/isijinternational.ISIJINT-2019-475.
[75] Arthur Seiji Nishikawa, pyebsd: an open-source tool for processing EBSD data and determining accurate orientation relationship. 2018. doi: 10.13140/RG.2.2.28920.19203. https://github.com/arthursn/pyebsd.
[76] Ju-Heon Kim, Dong-Ik Kim, Jong Seok Kim, Shi-Hoon Choi, Kyung-Woo Yi, and Kyu Hwan Oh, Technical investigation into the in-situ electron backscatter diffraction analysis for the recrystallization study on extra low carbon steels, Appl. Microsc., 43 (2): 88–97, June 2013. ISSN 2287-5123 doi: 10.9729/AM.2013.43.2.88.
[77] Martin Diehl, Lukas Kertsch, Konstantina Traka, Dirk Helm, Dierk Raabe, Site-specific quasi in situ investigation of primary static recrystallization in a low carbon steel, Mater. Sci. Eng.: A 755 (2019) 295–306, https://doi.org/10.1016/j.msea.2019.02.032. ISSN 09215093.
[78] F. Bachmann, Ralf Hielscher, Helmut Schaeben, Texture analysis with MTEX - Free and open source software toolbox, Solid State Phenom. 160 (2010) 63–68, https://doi.org/10.4028/www.scientific.net/SSP.160.63. ISSN 1662-9779.